

Electron-phonon superconductivity in CaBi_2 and the role of spin-orbit interaction.

Sylwia Gołab and Bartłomiej Wiendlocha*

Faculty of Physics and Applied Computer Science,

AGH University of Science and Technology, al. Mickiewicza 30, 30-059 Krakow, Poland

(Dated: April 2, 2019)

CaBi_2 is a recently discovered type-I superconductor with $T_c = 2$ K and a layered crystal structure. In this work electronic structure, lattice dynamics and electron-phonon interaction are studied, with a special attention paid to the influence of the spin-orbit coupling (SOC) on above-mentioned quantities. We find, that in the scalar-relativistic case (without SOC), electronic structure and electron-phonon interaction show the quasi-two dimensional character. Strong Fermi surface nesting is present, which leads to appearance of the Kohn anomaly in the phonon spectrum and enhanced electron-phonon coupling for the phonons propagating in the Ca-Bi atomic layers. However, strong spin-orbit coupling in this material changes the topology of the Fermi surface, reduces the nesting and the electron-phonon coupling becomes weaker and more isotropic. The electron-phonon coupling parameter λ is reduced by SOC almost twice, from 0.94 to 0.54, giving even stronger effect on the superconducting critical temperature T_c , which drops from 5.2 K (without SOC) to 1.3 K (with SOC). Relativistic values of λ and T_c remain in a good agreement with experimental findings, confirming the general need for including SOC in analysis of the electron-phonon interaction in materials containing heavy elements.

I. INTRODUCTION

Elemental bismuth has unusual electronic properties. It is a semimetal, crystallizing in a diatomic, rhombohedral structure, which is a result of a Peierls-Jones distortion [1]. Bi exhibits the strongest diamagnetism of all elements in the normal state (susceptibility $\chi \sim 10^{-5}$ emu) related to the large spin-orbit coupling effects [2], as it has the highest atomic number ($Z = 83$) of all non-radioactive elements. In its band structure one can find Dirac-like electronic states with small effective mass [2] and large mobility. Bismuth has very low charge carrier density of electrons and holes (about 10^{-5} carrier per atom) and its Fermi surface consists of three electronic and one hole pockets [3, 4]. As the electronic pockets lose their symmetry in the magnetic field, Bi was recently proposed as a "valleytronic" material, where contribution of each electronic pocket to the charge transport may be tuned by the magnetic field [5]. As far as the superconductivity is concerned, it was discovered long time ago, that amorphous bismuth is a superconductor with relatively high $T_c = 6$ K [6, 7]. On the other hand, crystalline bismuth was long considered not to be a superconductor, although finally it was found, that superconductivity occurs in ultra-low temperatures, below $T_c = 0.53$ mK [8].

There are many bismuth-based high-temperature superconductors, like $\text{Bi}_2\text{Sr}_2\text{CaCu}_2\text{O}_8$, where Bi_2O_2 layer plays a role of a charge reservoir [9]. Among the low-temperatures superconductors, we find several Bi-based families, including ABi_3 , with $A = \text{Sr}, \text{Ba}, \text{Ca}, \text{Ni}, \text{Co}, \text{La}$ [10–14], ABi with $A = \text{Li}, \text{Na}$ [15, 16], or ABi_2 with $A = \text{K}, \text{Rb}, \text{Cs}, \text{and Ca}$. In the last family, KBi_2 , RbBi_2 , and CsBi_2 , with $T_c = 3.6$ K, 4.25 K and 4.75 K respec-

tively, adopt cubic *fcc* structure [17], while our title compound CaBi_2 , with $T_c = 2.0$ K, is orthorhombic [18].

In recent years Bi compounds have attracted much attention as candidates for topological materials or topological superconductors. Among them we may find the well-known examples of semiconducting $\text{Bi}_{1-x}\text{Sb}_x$ alloy, or the "thermoelectric" tetradymites Bi_2Te_3 , Bi_2Se_3 [19, 20] and their relatives, like $\text{Sr}_x\text{Bi}_2\text{Se}_3$ [21]. Also A_3Bi_2 ($A = \text{Ca}, \text{Sr}, \text{Ba}$) compounds are considered as 3D topological insulators [22]. Moreover, topological states are present eg. in ThPtBi , ThPdBi and ThAuBi [23] (topological metals), HfIrBi [24] (topological semimetal), Bi_4I_4 [25] (quasi-1D topological insulator). All these examples show, that bismuth-based materials offer a variety of interesting physical properties, usually related to the strong relativistic effects.

In this work we focus on CaBi_2 compound, recently reported [18] to be a type-I superconductor, with $T_c = 2.0$ K. The key problem we would like to address is what is the effect of the spin-orbit coupling (SOC) on the electron-phonon interaction and superconductivity in this material. In order to do so, electronic structure, phonons and the electron-phonon coupling function are computed, in both scalar-relativistic [26] (without SOC) and relativistic (including SOC) way, and we found, that SOC indeed has a very strong impact on the computed quantities. In the scalar-relativistic case, electronic structure and electron-phonon interaction show the quasi-two dimensional character, with significantly enhanced electron-phonon coupling for the phonons propagating in the Ca-Bi atomic layers. However, strong spin-orbit coupling in this material changes the topology of the Fermi surface, indirectly making the electron-phonon interaction more three-dimensional and weaker, and the computed electron-phonon coupling constant λ is reduced nearly twice.

* wiendlocha@fis.agh.edu.pl

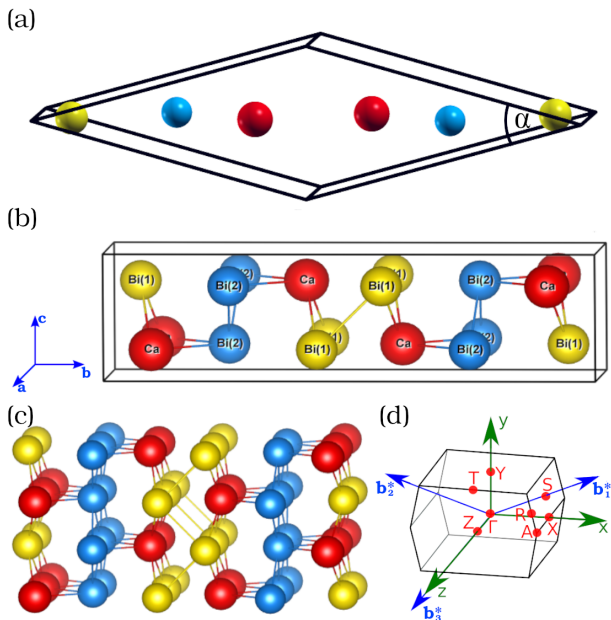


FIG. 1. The CaBi_2 crystal structure. Ca, Bi(1) and Bi(2) atoms are marked by red, yellow and blue balls, respectively. Panel (a) shows the primitive cell; (b) the conventional unit cell; (c) eight unit cells stacked to show the Ca-Bi(1) and Bi(2) atomic layers; (d) Brillouin zone of space group no. 63 with high-symmetry \mathbf{k} -points marked. \mathbf{b}^* are the reciprocal primitive vectors, while x, y, z are the Cartesian vectors in reciprocal space, parallel to the conventional unit cell $\mathbf{a}, \mathbf{b}, \mathbf{c}$ vectors.

II. COMPUTATIONAL DETAILS

CaBi_2 forms an orthorhombic ZrSi_2 -type structure (space group $Cmcm$, no. 63), which is shown in Fig. 1. The primitive cell of CaBi_2 is shown in Fig. 1(a) and contains 2 formula units (f.u.). There are two inequivalent positions of Bi atoms, denoted in this work as Bi(1) and Bi(2), whereas Ca atoms occupy one position. The base-centered conventional unit cell, shown in Fig. 1(b), contains 6 f.u. Relation between the conventional and primitive cells is visualized in Supplemental Material [27]. Experimental and theoretical [18] lattice parameters and atomic positions are shown in Table I. Conventional unit cell is elongated about 3.5 times along the b-axis, comparing to other dimensions. This is related to the quasi-two dimensional character of CaBi_2 crystal structure, with a sequence of atomic Bi(2) and Bi(1)-Ca layers, perpendicular to the b-axis, which form [Ca-Bi(1)]-[Bi(2)]-[Ca-Bi(1)] „sandwiches”. This quasi-2D geometry of the system, reflected also in the charge density distribution, was discussed in more details in Ref. [18].

Calculations in this work were done using the QUANTUM ESPRESSO software [28, 29], which is based on density-functional theory (DFT) and pseudopotential method. We used RRKJ (Rappe-Rabe-Kaxiras-Joannopoulos) ultrasoft pseudopotentials [30], with the PBE-GGA [31] (Perdew-Burke-Ernzerhof generalized

TABLE I. Theoretical and experimental [18] crystal structure parameters of CaBi_2 , space group $Cmcm$, no. 63. Theoretical values were obtained in scalar-relativistic calculations (w/o SOC) and relativistic calculations (w SOC), where for the latter case only atomic positions were relaxed, with a, b, c taken from the scalar-relativistic relaxation. All atoms occupy (4c) positions, $(0, y, 0.25)$, where y is given below. Conventional unit cell parameters are expressed in \AA units, primitive cell angle α is shown in Fig 1.

	a	b	c	α	$y\text{-Ca}$	$y\text{-Bi(1)}$	$y\text{-Bi(2)}$
expt.	4.696	17.081	4.611	30.74°	0.4332	0.0999	0.7552
w/o SOC	4.782	17.169	4.606	31.16°	0.4015	0.0655	0.7575
w SOC					0.4006	0.0668	0.7555

gradient approximation) for the exchange-correlation potential. For bismuth atom, both fully-relativistic and scalar-relativistic pseudopotentials were used, whereas for calcium only the scalar-relativistic pseudopotential was taken, as inclusion of SOC in its pseudopotential didn't affect the electronic structure of CaBi_2 . At first, unit cell dimensions and atomic positions were relaxed with BFGS (*Broyden-Fletcher-Goldfarb-Shanno*) algorithm, where the experimentally determined crystal structure parameters were taken as initial values (see, Table I). For the relativistic case (with SOC included), the unit cell dimensions were taken from the scalar-relativistic calculations, whereas the atomic positions were additionally relaxed. Next, the electronic structure was calculated on the Monkhorst-Pack grid of 12^3 \mathbf{k} -points. In the following step, the dynamical matrices were computed on the grid of 4^3 \mathbf{q} -points, using DFPT [32] (density-functional perturbation theory). Through double Fourier interpolation, real-space interatomic-force constants were obtained and used to compute the phonon dispersion relations. Finally, the Eliashberg electron-phonon interaction function $\alpha^2F(\omega)$ was calculated using the self-consistent first-order variation of the crystal potential from preceding phonon calculations, where summations over the Fermi surface was done using a dense grid of 24^3 \mathbf{k} -points. Obtained $\alpha^2F(\omega)$ was used to calculate the electron-phonon coupling constant λ in both scalar, and relativistic cases, and by using the Allen-Dynes equation [33], critical temperature was determined.

III. ELECTRONIC STRUCTURE

Electronic structure of CaBi_2 has been initially presented in Ref. [18], however for the sake of clarity and consistency of the present work it is briefly discussed also here. Fig. 2 shows electronic dispersion relations, densities of states (DOS) and Fermi surface (FS) of CaBi_2 . Brillouin zone of the system, with location of high-symmetry points, is shown in Fig. 1(d).

Fig. 2 shows both scalar- and full-relativistic results,

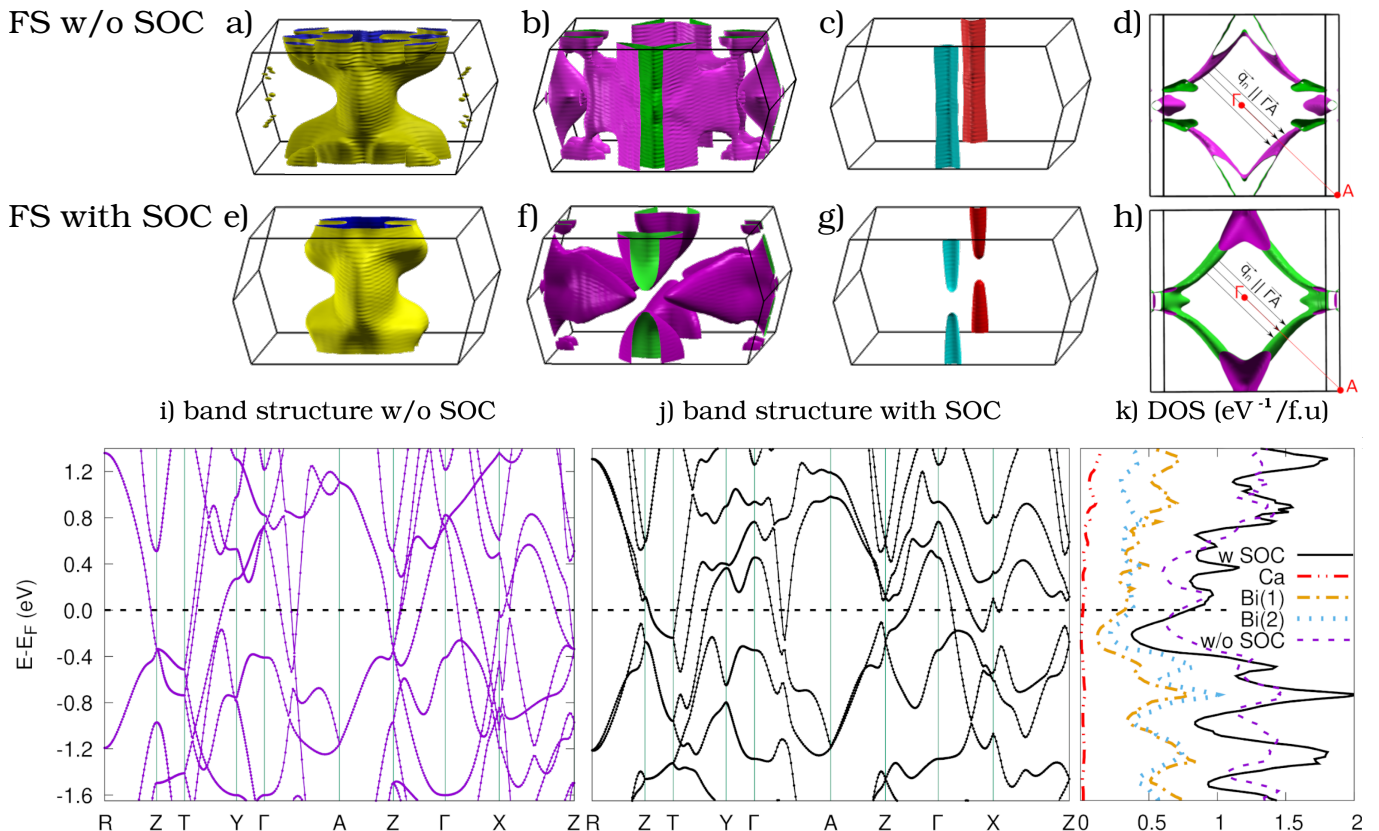


FIG. 2. The electronic structure of CaBi_2 without and with SOC: (a-c) and (e-g) three Fermi surface (FS) pieces; (d), (h) second FS piece with the nesting vector indicated; (i-j) electronic dispersion relations near the Fermi energy (E_F); (k) density of states (DOS), with the partial atomic densities plotted only for the relativistic case.

to visualize the influence of SOC on the electronic structure. As already mentioned [18], the studied system has a layered structure, with metallic Bi(2) layers and more ionic Ca-Bi(1) layers, stacked in [Ca-Bi(1)]-[Bi(2)]-[Ca-Bi(1)] „sandwiches” along the b -axis. This is reflected in the computed band structure, which is generally less-dispersive for the k_y direction, parallel to the b -axis (see bands e.g. in Γ -Y and Z-T directions), and more dispersive in others.

Three bands are crossing the Fermi level and form three pieces of Fermi surface, plotted in Fig. 2(a)-(d) for the scalar-relativistic case, and in Fig. 2(e)-(h) for the relativistic case. In general, the quasi-two dimensional structure of the system is seen in the topology of its Fermi surface, with the highlighted k_y direction, parallel to the real-space b axis, and perpendicular to atomic layers. In line with this, first piece [panels (a) and (e)] is cylindrical along k_y . The second piece [panels (b) and (f)] is large and rather complex, but also with a reduced dimensionality – there are large and flat FS areas parallel to k_y , while calculated without SOC. As there is a special \mathbf{q}_n vector, which connects flat areas of this part of Fermi surface, as shown in Fig. 2(d), this FS sheet exhibits strong nesting. The shortest nesting vector \mathbf{q}_n , which

lies in the Γ -A direction, is about $\frac{3}{4}$ of ΓA long, however, as seen in Fig. 2(d), nesting condition is also fulfilled for vectors longer than \mathbf{q}_n shown in the figure. Also, similar nesting condition is fulfilled for the Γ -A₁ direction, perpendicular to Γ -A. This piece of Fermi surface is most strongly influenced by the spin-orbit interaction, which splits it into separate sheets, considerably reducing the area of its flat parts. Thus, SOC reduces the quasi-two-dimensional character of FS and nesting becomes much weaker. Changes in topology of this FS piece are caused by the significant shift of the band along T-Z and opening of a gap around Z-point, seen in Fig. 2(i)-(j). Presence of the spin-orbital dependent Fermi surface nesting will have strong implications for the electron-phonon interaction, as will be discussed below. The third, smallest piece of Fermi surface, plotted in Fig. 2 (c) and (g), is also strongly two-dimensional and is changed by SOC in a similar way as the second one – without SOC it is nearly cylindrical along TZ direction (with no dispersion in k_y), while calculated with SOC, due to gap opening at Z-point, it is split into two cones.

The DOS plot in Fig. 2(k) clearly shows the main role of bismuth atoms in determining electronic properties of CaBi_2 , as most electronic states around the Fermi

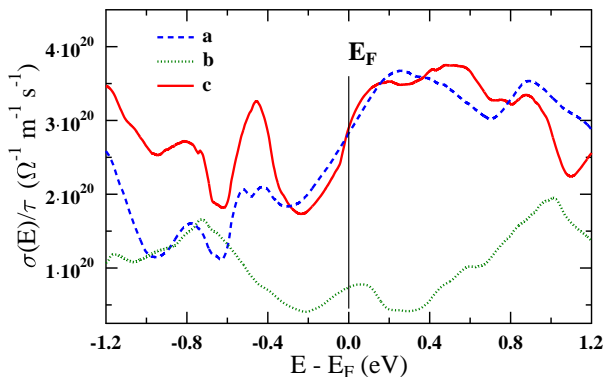


FIG. 3. Transport function of CaBi₂ computed in the constant scattering time approximation, along three unit cell directions.

level originate from bismuth 6p orbitals. SOC visibly modifies DOS as well, however, as far as the $N(E_F)$ value is concerned, the difference is not substantial, since $N(E_F) = 1.15 \text{ eV}^{-1}$ (with SOC) and $N(E_F) = 1.10 \text{ eV}^{-1}$ (without SOC).

To quantitatively investigate the quasi-2D electronic properties of CaBi₂, the electronic transport function of CaBi₂ was additionally computed, within the Boltzmann approach in the constant scattering time approximation (CSTA) and using the BOLTZTRAP code [34]. Fig. 3 shows the diagonal elements of the energy dependent electrical conductivity tensor of CaBi₂ (transport function $\sigma(E)$). For each band i and wave vector \mathbf{k} electrical conductivity is determined by the carrier velocity v and scattering time τ via $\sigma_{\alpha\beta}(i, \mathbf{k}) = e^2 \tau v_\alpha(i, \mathbf{k}) v_\beta(i, \mathbf{k})$. Electron velocities are related to the gradient of dispersion relations $E_i(\mathbf{k})$, $v_\alpha(i, \mathbf{k}) = \hbar^{-1} \partial E_i(\mathbf{k}) / \partial k_\alpha$, thus in the CSTA, by taking $\tau = \text{const.}$, one may compute $\sigma(E)/\tau$. The diagonal elements of $\sigma_{\alpha\beta}(i, \mathbf{k})$, integrated over the isoenergy surfaces, are shown in Fig. 3 as $\sigma_{\alpha\alpha}(E)/\tau$, where $\alpha = \{a, b, c\}$ are the three unit cell directions. As one can see, the generally less dispersive band structure along k_y direction in the Brillouin zone is responsible for the smaller electron velocities, making $\sigma(E)$ around E_F about four times smaller along b axis, than in the in-plane (a, c) directions.

IV. PHONONS

Figure 4 shows phonon dispersion relations $\omega(\mathbf{q})$ and phonon density of states $F(\omega)$, computed without and with SOC. Obtained phonon spectra are stable, i.e. with no imaginary frequencies in both cases. As in the primitive cell of CaBi₂ there are 6 atoms (2 f.u.), the total number of phonon branches is 18. Contributions of each of the atom to the phonon branches are marked using colored "fat bands", additionally partial phonon densities of states are computed. Due to the large difference in atomic masses ($M_{\text{Bi}} \simeq 209 \text{ u}$, $M_{\text{Ca}} \simeq 40 \text{ u}$) the phonon

TABLE II. The phonon frequency moments of CaBi₂, computed using Eq.(1)–(4).

	$\langle \omega^1 \rangle$	$\sqrt{\langle \omega^2 \rangle}$	$\langle \omega \rangle$	$\langle \omega_{\log} \rangle$	$\langle \omega_{\log}^{\alpha^2 F} \rangle$
		w/o SOC (THz)			
total	1.90	2.18	2.50	1.64	1.66
Ca	3.52	3.71	3.91	3.20	
Bi(1)	1.55	1.70	1.87	1.40	
Bi(2)	1.53	1.63	1.73	1.43	
		with SOC (THz)			
total	1.86	2.13	2.44	1.60	1.65
Ca	3.47	3.65	3.83	3.16	
Bi(1)	1.49	1.62	1.77	1.36	
Bi(2)	1.51	1.62	1.72	1.41	

spectrum is separated into two regions, with the low-frequency part, dominated by bismuth atoms' vibrations, and high-frequency part, dominated by calcium. Average total and partial phonon frequencies were computed using the formulas (1)–(4) given below, and are collected in Table II.

$$\langle \omega^n \rangle = \int_0^{\omega_{\max}} \omega^{n-1} F(\omega) d\omega \Big/ \int_0^{\omega_{\max}} F(\omega) \frac{d\omega}{\omega}, \quad (1)$$

$$\langle \omega \rangle = \int_0^{\omega_{\max}} \omega F(\omega) d\omega \Big/ \int_0^{\omega_{\max}} F(\omega) d\omega, \quad (2)$$

$$\langle \omega_{\log} \rangle = \exp \left(\int_0^{\omega_{\max}} F(\omega) \ln \omega \frac{d\omega}{\omega} \Big/ \int_0^{\omega_{\max}} F(\omega) \frac{d\omega}{\omega} \right), \quad (3)$$

$$\langle \omega_{\log}^{\alpha^2 F} \rangle = \exp \left(\int_0^{\omega_{\max}} \alpha^2 F(\omega) \ln \omega \frac{d\omega}{\omega} \Big/ \int_0^{\omega_{\max}} \alpha^2 F(\omega) \frac{d\omega}{\omega} \right). \quad (4)$$

Spin-orbit coupling has a visible impact on dynamical properties of CaBi₂. At first, SOC leads to slightly lower frequencies of phonons, since some of the calcium and bismuth modes are shifted towards lower ω . This is seen in phonon frequency moments, collected in Table II. However, the gap between the high- and low-frequency group of modes is increased, from about 0.7 THz without SOC, to 0.9 THz with SOC, i.e. frequencies of higher Bi modes are influenced to a larger degree, than the lower Ca branches.

Average phonon frequency $\langle \omega \rangle = 2.44 \text{ THz}$ (with SOC) corresponds to temperature of 117 K, lower than the experimentally determined Debye temperature $\Theta_D = 157 \text{ K}$ [18]. As there is no universal definition of the "theoretical" Debye temperature for a system with optical phonon branches, to be able to confront our calculations with the experimental findings, constant-volume lattice heat capacity C_V was calculated [35]:

$$C_V = R \int_0^{\infty} F(\omega) \left(\frac{\hbar\omega}{k_B T} \right)^2 \frac{\exp(\frac{\hbar\omega}{k_B T})}{(\exp(\frac{\hbar\omega}{k_B T}) - 1)^2} d\omega \quad (5)$$

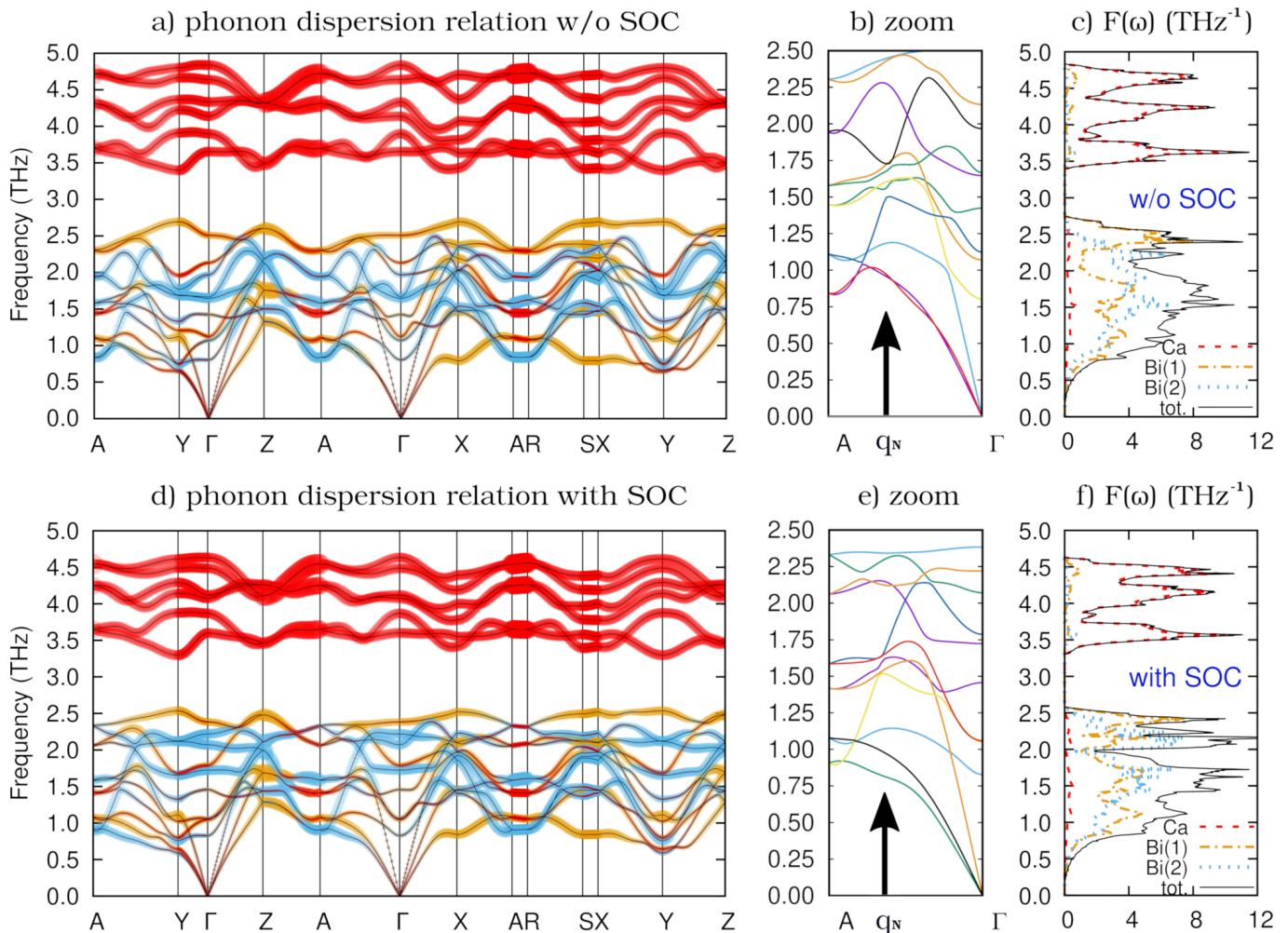


FIG. 4. Phonon dispersion relations and phonon DOS $F(\omega)$ of CaBi_2 without (at the top) and with (at the bottom) SOC. The contributions of atoms in dispersion relations in panels (a) and (d) are marked by colored fat bands; Ca - red, Bi(1) - yellow, Bi(2) - blue. The nesting vector \mathbf{q}_n , shown in Fig. 2, is marked with an arrow in panels (b,e).

using the relativistic phonon DOS $F(\omega)$ function. In Fig. 5 theoretical C_V is compared to the experimental constant-pressure C_p from Ref. [18] (electronic heat capacity was subtracted from C_p) and a good agreement is found. Deviation at higher temperatures most likely is due the difference of C_p and C_V , related to the anharmonic effects, where $C_p \simeq C_V(1 + \beta\gamma_G T)$ [35], where β is the volume thermal expansion coefficient and γ_G is the Grüneisen parameter. From the ratio of C_p/C_V at 300 K we can estimate $\beta\gamma_G \simeq 1.7 \cdot 10^{-4} \text{ K}^{-1}$. At low temperatures, where the difference between C_p and C_V should be small, we observe slightly larger calculated C_V , seen better in the C/T vs. T^2 plot in the inset in Fig. 5. Largest difference appears around $T \simeq 30$ K, and indicates slightly larger theoretical $F(\omega)$ in the 1 - 2 THz frequency range, than in the real system. However, still the largest differences between experimental and calculated values are of the order of 3-4%.

In the phonon spectrum, especially in the non-SOC case, we observe Kohn anomalies along Γ -A direction in

Fig. 4, where some of the phonon frequencies are strongly renormalized and lowered. This part of the spectrum is enlarged in Figs. 4(b,e) and one observes dips in the phonon branches, as well as the inflection of the acoustic mode, associated with Bi(2) vibrations, in the non-SOC spectrum. Similar inflection what was observed eg. in palladium [36]. In general, the Kohn anomaly [37] is an anomaly in the phonon dispersion curve in a metal, where the frequency of the phonon is lowered due to screening effects. Such an anomaly appears at the wave vector \mathbf{q}_n which satisfy the nesting conditions – when there are flat and parallel parts of Fermi surface, which can be connected by \mathbf{q}_n , there are many electronic states which may interact with phonons having the wavevector \mathbf{q}_n . In CaBi_2 , as we mentioned above, large parts of Fermi surface sheets, plotted in Figs. 2(b,f), may be connected by the same nesting vector \mathbf{q}_n , which is parallel to Γ -A direction, as is shown in Fig. 2(d,h) for scalar- and full-relativistic cases, respectively. This nesting vector is also marked with an arrow in the dispersion plots

in Fig. 4(b,e). Since in the scalar-relativistic case much larger parts of this Fermi surface sheet are parallel, nesting is much stronger and thus the anomalies are very pronounced in the non-SOC calculations, as seen in the dispersion plots in Fig. 4. The anomaly, observed here near the A-point, will have strong impact on electron-phonon interaction, as will be discussed in the next section.

V. ELECTRON-PHONON COUPLING

Electron-phonon interaction can be described in terms of the hamiltonian [35, 38]:

$$\hat{H}_{e-p} = \sum_{\mathbf{k}, \mathbf{q}, \nu} g_{\mathbf{q}\nu}(\mathbf{k}, i, j) c_{\mathbf{k}+\mathbf{q}}^{\dagger i} c_{\mathbf{k}}^j (b_{-\mathbf{q}\nu}^{\dagger} + b_{\mathbf{q}\nu}), \quad (6)$$

The creation and annihilation operators $c_{\mathbf{k}+\mathbf{q}}^{\dagger i}$, $c_{\mathbf{k}}^j$ refer to electrons in the state $\mathbf{k}+\mathbf{q}$ and \mathbf{k} in the i -th and j -th band respectively, while $b_{-\mathbf{q}\nu}^{\dagger}$, $b_{\mathbf{q}\nu}$ operators describe emission or absorption of the phonon from the ν -th mode and with wave vectors $-\mathbf{q}$ or \mathbf{q} , respectively. The electron-phonon interaction matrix elements $g_{\mathbf{q}\nu}(\mathbf{k}, i, j)$ have the form

$$g_{\mathbf{q}\nu}(\mathbf{k}, i, j) = \left(\frac{\hbar}{2M\omega_{\mathbf{q}\nu}} \right)^{1/2} \langle \psi_{i,\mathbf{k}} | \frac{dV_{\text{SCF}}}{d\hat{u}_{\nu}} \cdot \hat{\epsilon}_{\nu} | \psi_{j,\mathbf{k}+\mathbf{q}} \rangle. \quad (7)$$

Here $\omega_{\mathbf{q}\nu}$ is the frequency of ν -th phonon mode at \mathbf{q} -point, $\psi_{i,\mathbf{k}}$ is an electron wave function at \mathbf{k} -point, $\hat{\epsilon}_{\nu}$ is a phonon polarization vector and $\frac{dV_{\text{SCF}}}{d\hat{u}_{\nu}}$ is a change of electronic potential, calculated in the self-consistent cycle, due to the displacement of an atom, \hat{u}_{ν} . On this basis one can calculate the phonon linewidth

$$\begin{aligned} \gamma_{\mathbf{q}\nu} = & 2\pi\omega_{\mathbf{q}\nu} \sum_{ij} \int \frac{d^3k}{\Omega_{\text{BZ}}} |g_{\mathbf{q}\nu}(\mathbf{k}, i, j)|^2 \\ & \times \delta(E_{\mathbf{q},i} - E_F) \delta(E_{\mathbf{k}+\mathbf{q},j} - E_F), \end{aligned} \quad (8)$$

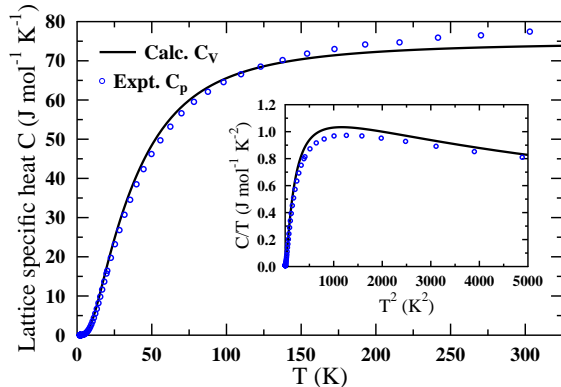


FIG. 5. Computed constant volume C_V (lines) and measured constant pressure C_p [18] (points) lattice heat capacity of CaBi_2 , given per formula unit.

TABLE III. Frequencies $\omega_{\nu\mathbf{q}}$ (THz) and linewidths $\gamma_{\nu\mathbf{q}}$ (GHz) of eighteen, doubly-degenerated phonon modes ν at the \mathbf{q} -point A, obtained in scalar-relativistic (scalar) and relativistic (rel) calculations.

ν	1-2	3-4	5-6	7-8	9-10	11-12	13-14	15-16	17-18
ω_{scalar}	0.84	1.10	1.44	1.57	1.93	2.29	3.68	4.29	4.69
ω_{rel}	0.91	1.08	1.42	1.59	2.06	2.33	3.65	4.25	4.54
γ_{scalar}	1.9	39.4	67.5	13.3	8.3	48.9	29.7	37.9	15.8
γ_{rel}	0.6	0.5	0.3	0.8	2.0	1.9	0.9	0.9	1.2

where $E_{\mathbf{k},i}$ refers to the energy of an electron. The phonon linewidth describes the strength of the interaction of the electron at the Fermi surface with the phonon from the ν -th mode, which has the wave vector \mathbf{q} , and it is inversely proportional to the lifetime of the phonon. Now, the Eliashberg function can be defined as

$$\alpha^2 F(\omega) = \frac{1}{2\pi N(E_F)} \sum_{\mathbf{q}\nu} \delta(\omega - \omega_{\mathbf{q}\nu}) \frac{\gamma_{\mathbf{q}\nu}}{\hbar\omega_{\mathbf{q}\nu}}. \quad (9)$$

where $N(E_F)$ refers to the electronic DOS at Fermi level. The Eliashberg function is proportional to the sum over all phonon modes and all \mathbf{q} -vectors of phonon linewidths divided by their energies, and describes the interaction of electrons from the Fermi surface with phonons having frequency ω . The total electron-phonon coupling parameter λ may be now defined using the $\alpha^2 F(\omega)$ function, as:

$$\lambda = 2 \int_0^{\omega_{\text{max}}} \frac{\alpha^2 F(\omega)}{\omega} d\omega, \quad (10)$$

or alternatively, directly by the phonon linewidths:

$$\lambda = \sum_{\mathbf{q},\nu} \frac{\gamma_{\mathbf{q}\nu}}{\pi\hbar N(E_F)\omega_{\mathbf{q},\nu}^2}. \quad (11)$$

More detailed description of the theoretical aspects of the electron-phonon coupling can be found in [35, 38].

Figures 6(a,d) display the phonon dispersion curves, with shading corresponding to the phonon linewidth $\gamma_{\mathbf{q}\nu}$ (in THz units) for the mode ν at \mathbf{q} -point. To make $\gamma_{\mathbf{q}\nu}$ visible for the SOC case, $\gamma_{\mathbf{q}\nu}$ is multiplied by 4, and the same multiplier is kept on both panels (a,d) to ensure the same visual scale. Eliashberg function $\alpha^2 F(\omega)$, plotted on the top of phonon DOS, $F(\omega)$, is shown in panels (b,e), and $\alpha^2 F(\omega)$ decomposed over the 18 phonon modes in panels (c,f). In panels (b,e), Eliashberg function is renormalized to $3n$ (n - number of atoms in the primitive cell), in the same way as phonon DOS, to allow for a direct comparison of both functions. Each of the quantities is plotted as obtained from scalar-relativistic calculations [Fig. 6(a,b,c)], and full-relativistic calculations [Fig. 6(e,f,g,h)]. The finite width of the phonon lines, according to Eq.(11), is a measure of a local strength of the electron-phonon interaction. One thing that immediately

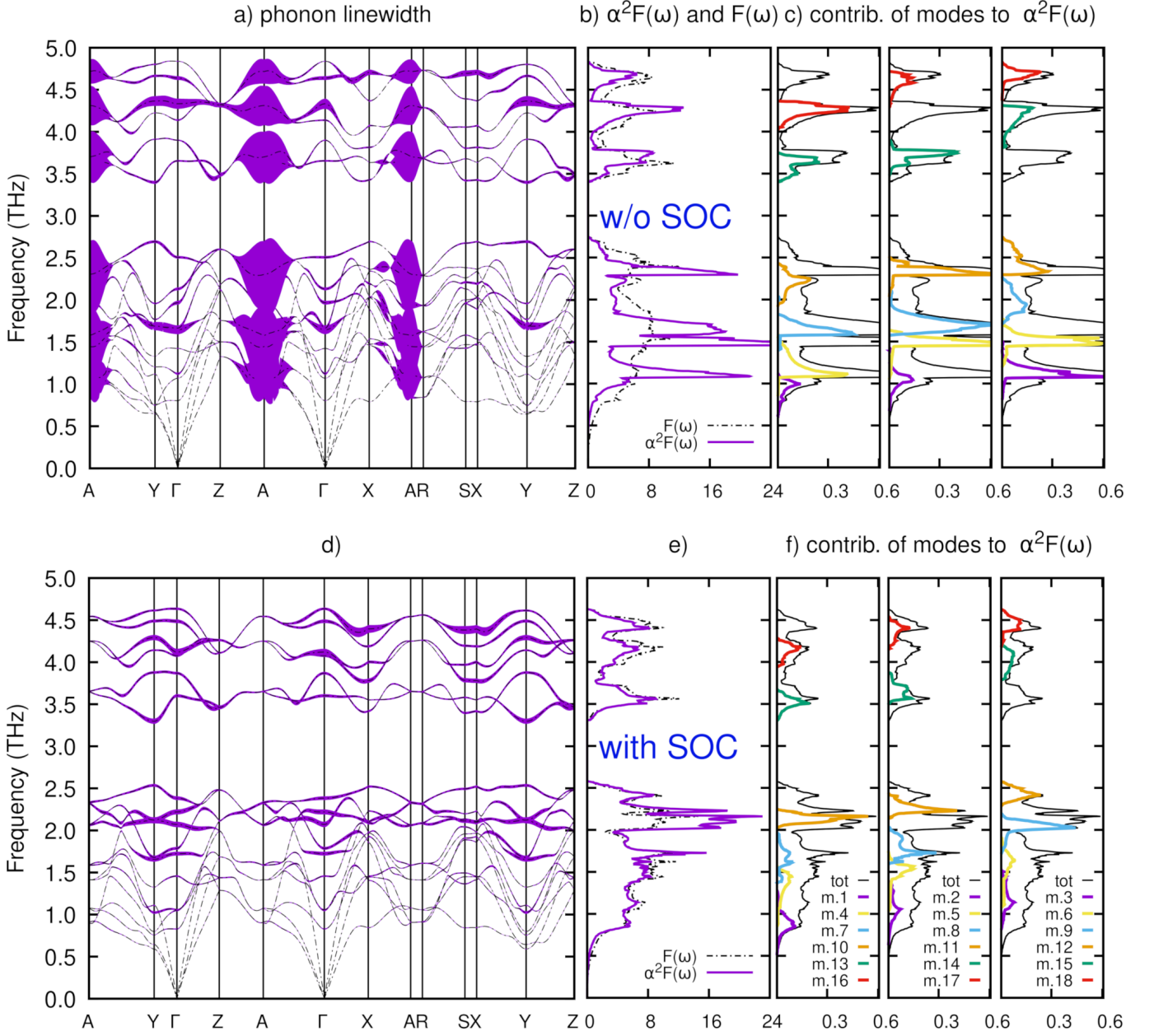


FIG. 6. Electron-phonon coupling in CaBi_2 ; (a-c) without SOC, (d-f) with SOC. Phonon dispersion relations with shading corresponding to phonon linewidth $\gamma_{\mathbf{q}\nu}$ [panels (a,d)]. In both panels (a,d), $\gamma_{\mathbf{q}\nu}$ (in THz units) is multiplied by 4, to make it visible for the SOC case. Panels (b,e) show the Eliashberg function $\alpha^2 F(\omega)$, renormalized to $3n$ ($n = 6$ is the number of atoms in the primitive cell), with the phonon DOS $F(\omega)$ plotted in the background; panels (c,f) show the actual $\alpha^2 F(\omega)$ with decomposition over all the 18 phonon modes.

catches the eye is a huge phonon linewidth $\gamma_{\mathbf{q}\nu}$ around the A-point in the scalar-relativistic results in Fig. 6(a). This large $\gamma_{\mathbf{q}\nu}$ area starts at the nesting vector \mathbf{q}_n and is related to the presence of the Kohn anomaly and Fermi surface nesting. The large number of electronic states, which may interact with phonons having wavevectors from this area of the Brillouin zone, makes the electron-phonon interaction strong and anisotropic. Comparing Fig. 6(a) and Fig. 4(a) we also see, that the strong

electron-phonon interaction around the A point is related to the Ca and Bi(1) atoms vibrations, with much smaller contribution from Bi(2) atomic modes. These strong-coupling modes involve both in-plane and out-of-plane Ca and Bi(1) atomic displacements, as can be seen in the displacement patterns shown in Supplemental Material [39], however the corresponding phonon wave vectors are confined to the in-plane $q_x - q_z$ directions. This is correlated with the quasi-2D layered structure of this com-

pound and shows signatures of the two-dimensional character of the electron-phonon interaction here. Frequencies and phonon linewidths $\gamma_{\mathbf{q}\nu}$ of all doubly-degenerated phonon modes in A-point are shown in Table III.

The strong anisotropy and mode-dependence of the electron-phonon interaction in CaBi_2 in the scalar-relativistic case results in the Eliashberg function having significantly different shape, than the phonon DOS function $F(\omega)$, as seen in Fig. 6(b). $\alpha^2F(\omega)$ is strongly peaked around the seven frequencies of phonon modes from the A-point, which have large $\gamma_{\mathbf{q}\nu}$. Contributions of each of the total number of 18 phonon modes to the total $\alpha^2F(\omega)$ function are plotted in Fig. 6(c), and λ_ν values are collected in Table IV. Total electron-phonon coupling constant is directly calculated from the Eliashberg function, using Eq.(10), which gives $\lambda = 0.94$. This value is considerably larger, than expected from the experimental value of T_c via inverted McMillan formula [40] $\lambda = 0.53$. The latter value is calculated using the experimental Debye temperature $\Theta_D = 157$ K [18], and assuming Coulomb pseudopotential parameter $\mu^* = 0.10$, since CaBi_2 is a simple metal with s and p electrons and low $N(E_F)$ value [41]. Also, λ may be extracted in an usual way from the experimental value of the electronic heat capacity coefficient $\gamma_{\text{expt}} = 4.1$ mJ/(mol K²) and calculated $\gamma_{\text{calc}} = \frac{\pi^2}{3} k_B^2 N(E_F)$, where k_B is the Boltzmann constant and $N(E_F)$ is the DOS at the Fermi level, if one assumes that the measured Sommerfeld coefficient γ_{expt} is renormalized by the electron-phonon interaction only:

$$\lambda = \frac{\gamma_{\text{expt}}}{\gamma_{\text{calc}}} - 1. \quad (12)$$

This gives $\gamma_{\text{calc}} = 2.59$ mJ/(mol K²) and similar value of $\lambda = 0.58$, much smaller, than $\lambda = 0.94$ obtained in the scalar-relativistic calculations.

When spin-orbit coupling is included, however, due to the change in Fermi surface shape and reduction of the area of flat parts of FS, connected by the nesting vector \mathbf{q}_n [see, Fig. 2(b,f)], the overall strength of the electron-phonon interaction is reduced, both in relation to the A-point area, and to the total λ . As can be seen in Figs. 6(e,f), in this case electron-phonon interaction becomes less mode- and \mathbf{q} -dependent, and huge $\gamma_{\mathbf{q}\nu}$ around A-point are absent. From the values of the phonon frequencies and linewidths at the A-point, collected in Table III, we precisely see the strong impact of SOC on the electron-phonon interaction: relatively small changes in phonon frequencies ω are followed by a reduction of $\gamma_{\mathbf{q}\nu}$ by a factor 10 to 100. As now the coupling of electrons to those planar phonon modes is not enhanced any more, in the relativistic case the electron-phonon interaction is more three-dimensional and weakly depends on frequency, and thus the Eliashberg function now closely follows the phonon DOS $F(\omega)$ function, as presented in Fig. 6(e). The relative enhancement of the electron-phonon coupling occurs for the last three optic modes from the lower-frequency part of the spectrum before the gap. These are modes no. 10, 11 and 12 in Fig. 6(f),

located between 2.0 and 2.2 THz. Atomic displacement patterns for these modes in Y point, where the phonon linewidths are relatively large, are shown in Supplemental Material [42]. In the mode no. 12 we find Bi(1) and Ca vibrations perpendicular to atomic layers, whereas in modes 11 and 10 mostly Bi(2) atoms are involved in the in-plane vibrations. Due to overlap of these three modes in 2.0-2.2 THz frequency range, coupling is here enhanced and $\alpha^2F(\omega)$ is above the bare DOS function $F(\omega)$, if both are normalized to the same value ($3n$ in Fig. 6(e)). But if we take a look at Table IV, due to strong dependence of λ also on the phonon frequency in Eq.(11), $\lambda \propto \omega^{-2}$, the largest contributions per phonon mode come from the 1st, lowest acoustic mode and from the 9th optic mode, which involves Ca and Bi(1) vibrations.

The cumulative frequency distribution of λ is shown in Fig. 7. For both, scalar and relativistic case, main contribution to the electron-phonon coupling constant comes from the phonon modes, located between 1.0 and 2.5 THz. For the scalar-relativistic case, $\lambda(\omega)$ has three steps, due to peaks in the Eliashberg function, appearing before the gap of the phonon spectrum in Fig. 6. When the spin-orbit coupling is included, as has been mentioned above, electron-phonon interaction becomes less frequency-dependent, thus $\lambda(\omega)$ is nearly a linear function in this frequency range. As ω increases above the gap, the relative contribution of the higher energy modes to λ become small, as almost 90% of the total λ is provided by phonons with $\omega < 2.5$ THz.

Now, moving to the total electron-phonon coupling parameter, in the relativistic case $\lambda = 0.54$, which is now in an excellent agreement with the above-mentioned values, determined from the experimental T_c ($\lambda = 0.53$), as well as from the Sommerfeld parameter renormalization factor ($\lambda = 0.51$, when taking the relativistic $N(E_F)$ value). These numbers are summarized in Table V.

Using the calculated λ and $\langle \omega_{\log}^{\alpha^2 F} \rangle$ values, and the Allen-Dynes [33] formula:

$$k_B T_c = \frac{\hbar \langle \omega_{\log}^{\alpha^2 F} \rangle}{1.20} \exp \left\{ - \frac{1.04(1 + \lambda)}{\lambda - \mu^*(1 + 0.62\lambda)} \right\} \quad (13)$$

superconducting critical temperatures are calculated and included in Table V. The Coulomb pseudopotential parameter was kept at $\mu^* = 0.10$. As in the case of λ , in

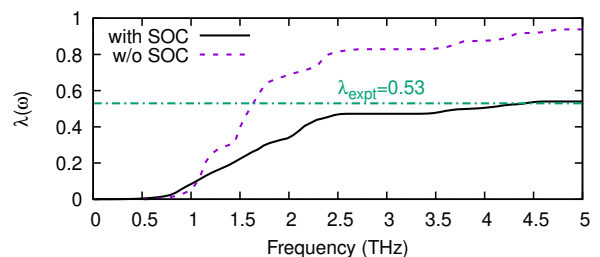


FIG. 7. The cumulative frequency distribution of λ , defined as: $\lambda(\omega) = 2 \int_0^\omega \alpha^2 F(\Omega) \frac{d\Omega}{\Omega}$, for scalar and relativistic cases.

TABLE IV. Contributions to the total electron-phonon coupling constant λ from each of the eighteen phonon branches of CaBi₂, the total $\lambda = \sum_{\nu} \lambda_{\nu}$.

mode no.	1	2	3	4	5	6	7	8	9	10	11	12	13	14	15	16	17	18	total λ
λ_{ν} w/o SOC	0.04	0.05	0.10	0.10	0.09	0.09	0.07	0.11	0.04	0.03	0.05	0.04	0.02	0.02	0.02	0.03	0.01	0.01	0.94
λ_{ν} w SOC	0.06	0.04	0.04	0.04	0.04	0.04	0.03	0.04	0.05	0.04	0.03	0.02	0.01	0.01	0.01	0.01	0.01	0.01	0.54

the scalar-relativistic calculations obtained value of the critical temperature $T_c = 5.2$ K is considerably above the experimental $T_c = 2.0$ K. Better agreement with experiment is reached after including the spin-orbit coupling, as it lowers computed T_c to 1.3 K, only slightly lower than the experimental one.

Our calculations show that in CaBi₂ the spin-orbit coupling has a very strong and detrimental effect on the electron-phonon interaction and superconductivity. This effect is indirect here, as is caused by the reduction of the Fermi surface nesting, which leads to important changes in ω - and \mathbf{q} -dependence of the electron-phonon interaction. As a result, which SOC electron-phonon interaction is more three-dimensional and isotropic, comparing to the scalar-relativistic case. SOC effectively weakens the electron-phonon coupling by 42%: from $\lambda_{\text{scalar}} = 0.94$ to $\lambda_{\text{rel}} = 0.54$. This underlines the need of including SOC in calculations of the electron-phonon coupling in compounds based on such heavy elements, like bismuth, where SOC strongly affects Fermi surface of the material.

In Table VI we have gathered available computational and experimental data on a number of related binary intermetallic superconductors containing Bi. Comparing our results to those reported recently for ABi₃ ($A = \text{Ba}, \text{Sr}, \text{La}$) we notice, that SOC effect on the electron-phonon interaction and superconductivity in CaBi₂ is stronger, if the relative change between the calculated λ_{scalar} and λ_{rel} is taken as an indicator. Moreover, in CaBi₂ the effect is opposite, since in ABi₃ SOC enhances the electron-phonon interaction, λ and T_c . What is worth noting here, except for CaBi₂, there are large differences in λ values, obtained from experimental T_c via McMillan equation, and from the Sommerfeld electronic heat capacity coefficient and computed $N(E_F)$ values (Eq. 12). For the two cases of KBi₂ and BaBi₃, the computed γ_{calc} values

TABLE V. Electron-phonon coupling constant λ and critical temperature T_c calculated for CaBi₂ without SOC [w/o SOC]; with SOC [w SOC]; extracted from the experimental data using T_c and the McMillan formula [expt. (T_c)]; extracted from the experimental data using electronic heat capacity coefficient γ and theoretical $N(E_F)$ with SOC [expt. (γ)].

	w/o SOC	w SOC	expt. (T_c)	expt. (γ)
$N(E_F)$ (eV ⁻¹)	1.10	1.15		
λ	0.94	0.54	0.53	0.51
T_c (K)	5.2	1.3	2.0	

are even larger than the measured γ_{expt} , making λ negative, and showing that those systems require reinvestigation. Especially BaBi₃, where two other reported values of $\gamma_{\text{expt}} > 40$ mJ/(mol K²) are large beyond expectations, and also result in spurious values of $\lambda \sim 6 - 7$ [53].

VI. SUMMARY AND CONCLUSIONS

First principles calculations of the electronic structure, phonons and the electron-phonon coupling function have been reported for the intermetallic superconductor CaBi₂. Calculations were performed within the scalar-relativistic (without the spin-orbit coupling) and relativistic (with spin-orbit coupling) approach, which allowed us to discuss the SOC effect on the computed physical properties. Electronic structure and electronic transport function reflect the quasi-2D layered structure of the studied compound. Dynamic spectrum of CaBi₂ is separated into two parts, dominated by the heavier (Bi) and lighter (Ca) atoms' vibrations. Strong influence of SOC on the electron-phonon interaction was found. In the scalar-relativistic case, due to strong nesting between the flat sheets of the Fermi surface and presence of a large Kohn anomaly, electron-phonon interaction is enhanced in the vicinity of the A point in the Brillouin zone. This enhancement of the electron-phonon interaction has a two-dimensional character, as electrons from the flat parts of FS are strongly coupled to phonons, propagating in $q_x - q_z$ directions, and which involve displacement of atoms from the Ca-Bi(1) layers. When SOC is included, however, due to the change in Fermi surface topology, nesting becomes weaker and the electron-phonon coupling becomes more isotropic and less ω -dependent. As a result, SOC reduces the magnitude of the electron-phonon coupling in about 42%, from $\lambda_{\text{scalar}} = 0.94$ to $\lambda_{\text{rel}} = 0.54$, in an opposite way to related ABi₃ superconductors. Critical temperature, calculated using the Allen-Dynes equation and relativistic electron-phonon coupling constant gives $T_c = 1.3$ K. The computed relativistic values of λ and T_c remain in a good agreement with experimental results, where $T_c = 2.0$ K and $\lambda = 0.51$ (from the Sommerfeld parameter renormalization) or $\lambda = 0.53$ (from T_c , Θ_D and McMillan equation). Our results confirm the need of including the spin-orbit coupling in calculations of the electron-phonon interaction functions for materials containing such heavy elements, like Bi, and where SOC strongly modifies Fermi surface of the system. Finally we may summarize, that CaBi₂ is a moderately coupled electron-phonon super-

TABLE VI. Experimental and theoretical data for selected binary Bi-based superconductors. λ_{calc} and T_c are calculated from DFT in a scalar-relativistic (scalar) and relativistic (rel) way; $\lambda(T_c)$ is calculated from experimental T_c , McMillan formula, Debye temperature Θ_D and taking $\mu^* = 0.10$; $\lambda(\gamma_{\text{expt}})$ is computed using Eq.(12) from experimental Sommerfeld parameter γ_{expt} and theoretical "bare" value of $N(E_F)$, as given in referenced literature.

	Space group	$\lambda_{\text{calc}}^{\text{scalar}}$	$\lambda_{\text{calc}}^{\text{rel}}$	γ_{expt} ($\frac{\text{mJ}}{\text{molK}^2}$)	$\lambda(T_c)$	$\lambda(\gamma_{\text{expt}})$	T_c^{scalar} (K)	T_c^{rel} (K)	T_c^{expt} (K)	Θ_D (K)	Ref.
CaBi ₂	<i>CmCm</i>	0.94	0.54	4.1	0.53	0.51	5.2	1.3	2.0	157	this work, [18]
KBi ₂	<i>Fd3m</i>	0.76		1.3	0.70	0.7	2.73		3.6	123	[43][44]
NaBi	<i>P4/mmm</i>			3.4	0.56	1.05			2.1	140	[16]
BaBi ₃	<i>Fd3m</i>			3.2	0.76	-0.43			6.0	171	[45]
			1.43	41	0.83	6.25		5.29	5.9	142	[10, 46]
				49.2	0.81	7.70			5.9	149	[47]
SrBi ₃	<i>Pm3m</i>	0.91	1.1	14	0.91	1.74	3.73	5.15	5.5	111	[10, 48]
				6.5	0.72	0.27			5.6	180	[45]
				11	0.72	1.16			5.5	180	[47]
LaBi ₃	<i>Pm3m</i>	0.90	1.35				3.71	6.88	7.3		[13, 49]
CaBi ₃	<i>Pm3m</i>	1.23					5.16		1.7		[11, 50]
CoBi ₃	<i>Pnma</i>			16.7	0.41	1.19			0.5	124	[14]
NiBi ₃	<i>Pnma</i>			12.7	0.70	1.45			4.1	141	[12, 51]
				11.1	0.73	1.14				128	[12, 52]

conductor with strong spin-orbit coupling effects on its physical properties.

VII. ACKNOWLEDGMENTS

This work was partly supported by the National Science Center (Poland), grant No. 2017/26/E/ST3/00119,

and by the AGH-UST statutory tasks No. 11.11.220.01/5 within subsidy of the Ministry of Science and Higher Education.

-
- [1] H. Jones, "Applications of the Bloch Theory to the Study of Alloys and of the Properties of Bismuth," *Proceedings of the Royal Society of London A* **147**, 396–417 (1934).
- [2] Y. Fuseya, M. Ogata, and H. Fukuyama, "Transport Properties and Diamagnetism of Dirac Electrons in Bismuth," *Journal of the Physical Society of Japan* **84**, 012001 (2015).
- [3] V. S. Édel'Man and M. S. Khaïkin, "Investigation of the Fermi Surface in Bismuth by Means of Cyclotron Resonance," *Soviet Journal of Experimental and Theoretical Physics* **22**, 77 (1966).
- [4] Hyungyu Jin, Bartłomiej Wiendlocha, and Joseph P. Heremans, "P-type doping of elemental bismuth with indium, gallium and tin: a novel doping mechanism in solids," *Energy Environ. Sci.* **8**, 2027–2040 (2015).
- [5] Z. Zhu, A. Collaudin, B. Fauqué, W. Kang, and K. Behnia, "Field-induced polarization of Dirac valleys in Bismuth," *Nature Physics* **8**, 89–94 (2012), arXiv:1109.2774 [cond-mat.str-el].
- [6] W. Buckel and R. Hilsch, "Einfluß der Kondensation bei tiefen Temperaturen auf den elektrischen Widerstand und die Supraleitung für verschiedene Metalle," *Zeitschrift für Physik* **138**, 109–120 (1954).
- [7] Zaahel Mata-Pinzón, Valladares Ariel A., Valladares Renela M., and Valladares Alexander, "Superconductivity in Bismuth. A New Look at an Old Problem," *PLOS ONE* **11**, 1–20 (2016).
- [8] Om Prakash, Anil Kumar, A. Thamizhavel, and S. Ramakrishnan, "Evidence for bulk superconductivity in pure bismuth single crystals at ambient pressure," *Science* **355**, 52–55 (2017).
- [9] V. F. Shamrai, "Crystal Structures and Superconductivity of Bismuth High Temperature Superconductors (Review)," *Inorganic Materials: Applied Research* **4**, 273 (2013).
- [10] D. F. Shao, X. Luo, W. J. Lu, L. Hu, X. D. Zhu, W. H. Song, X. B. Zhu, and Y. P. Sun, "Spin-orbit coupling enhanced superconductivity in Bi-rich compounds ABi₃ (A = Sr and Ba)," *Scientific Reports* **6**, 21484 (2016).
- [11] B. T. Matthias and J. K. Hulm, "A Search for New Superconducting Compounds," *Phys. Rev.* **87**, 799–806 (1952).
- [12] Elena Gati, Li Xiang, Lin-Lin Wang, Soham Manni, Paul C Canfield, and Sergey L Budko, "Effect of pressure on the physical properties of the superconductor NiBi₃," *Journal of Physics: Condensed Matter* **31**, 035701 (2018).
- [13] Tatsuya Kinjo, Saori Kajino, Taichiro Nishio, Kenji Kawashima, Yousuke Yanagi, Izumi Hase, Takashi Yanagisawa, Shigeyuki Ishida, Hijiri Kito, Nao Takeshita, *et al.*, "Superconductivity in LaBi₃ with AuCu₃-type structure," *Superconductor Science and Technology* **29**, 03LT02 (2016).

- [14] Sophie Tencé, Oleg Janson, Cornelius Krellner, Helge Rosner, Ulrich Schwarz, Y Grin, and F Steglich, “CoBi₃ - the first binary compound of cobalt with bismuth: high-pressure synthesis and superconductivity,” *Journal of Physics: Condensed Matter* **26**, 395701 (2014).
- [15] Takashi Sambongi, “Superconductivity of LiBi,” *Journal of the Physical Society of Japan* **30**, 294–294 (1971).
- [16] SK Kushwaha, JW Krizan, Jun Xiong, Tomasz Klimczuk, QD Gibson, Tian Liang, NP Ong, and RJ Cava, “Superconducting properties and electronic structure of NaBi,” *Journal of Physics: Condensed Matter* **26**, 212201 (2014).
- [17] B. W. Roberts, “Survey of superconductive materials and critical evaluation of selected properties,” *Journal of Physical and Chemical Reference Data* **5**, 581–822 (1976).
- [18] M.J. Winarski, B. Wiendlocha, S. Golab, S. K. Kushwaha, P. Wiśniewski, D. Kaczorowski, J. D. Thompson, R. J. Cava, and T. Klimczuk, “Superconductivity in CaBi₂,” *Physical Chemistry Chemical Physics* **18(31)**, 21737 (2016).
- [19] M Zahid Hasan and Charles L Kane, “Colloquium: topological insulators,” *Reviews of modern physics* **82**, 3045 (2010).
- [20] J. P. Heremans, R. J. Cava, and N. Samarth, “Tetradymites as thermoelectrics and topological insulators,” *Nature Reviews Materials* **2**, 17049 (2017).
- [21] Guan Du, Jifeng Shao, Xiong Yang, Zengyi du, Delong Fang, Changjing Zhang, Jinghui Wang, Kejing Ran, Jinsheng Wen, Huan Yang, Yuheng Zhang, and Hai-Hu Wen, “Drive the Dirac electrons into Cooper pairs in Sr_xBi₂Se₃,” *Nature communications* **8**, 14466 (2017).
- [22] Ronghan Li, Qing Xie, Xiyue Cheng, Dianzhong Li, Yiyi Li, and Xing-Qiu Chen, “First-principles study of the large-gap three-dimensional topological insulators M₃Bi₂ (M= Ca, Sr, Ba),” *Physical Review B* **92**, 205130 (2015).
- [23] Zahra Nourbakhsh and Aminollah Vaez, “Electronic properties and topological phases of Th XY (X = Pb, Au, Pt and Y = Sb, Bi, Sn) compounds,” *Chinese Physics B*, **25**, 037101 (2016).
- [24] Guangtao Wang and JunHong Wei, “Topological phase transition in half-Heusler compounds HfIrX (X=As, Sb, Bi),” *Computational Materials Science* **124**, 311 – 315 (2016).
- [25] Huaqing Huang and Wenhui Duan, “Topological insulators: Quasi-1D topological insulators,” *Nature Materials*, **15**, 129–130 (2016).
- [26] Dale Koelling and B N Harmon, “A technique for relativistic spin-polarized calculations,” *Journal of Physics C: Solid State Physics*, **10**, 3107 (1977).
- [27] See Fig. S1 in Supplemental Material for the relation between the conventional and primitive cells.
- [28] Paolo Giannozzi, Stefano Baroni, Nicola Bonini, Matteo Calandra, Roberto Car, Carlo Cavazzoni, Davide Ceresoli, Guido L Chiarotti, Matteo Cococcioni, Ismaila Dabo, Andrea Dal Corso, Stefano de Gironcoli, Stefano Fabris, Guido Fratesi, Ralph Gebauer, Uwe Gerstmann, Christos Gougousis, Anton Kokalj, Michele Lazzeri, Layla Martin-Samos, Nicola Marzari, Francesco Mauri, Riccardo Mazzarello, Stefano Paolini, Alfredo Pasquarello, Lorenzo Paulatto, Carlo Sbraccia, Sandro Scandolo, Gabriele Sclauzero, Ari P Seitsonen, Alexander Smogunov, Paolo Umari, and Renata M Wentzcovitch, “QUANTUM ESPRESSO: a modular and open-source software project for quantum simulations of materials,” *Journal of Physics: Condensed Matter* **21**, 395502 (19pp) (2009).
- [29] P Giannozzi, O Andreussi, T Brumme, O Bunau, M Buongiorno Nardelli, M Calandra, R Car, C Cavazzoni, D Ceresoli, M Cococcioni, N Colonna, I Carnimeo, A Dal Corso, S de Gironcoli, P Delugas, R A DiStasio Jr, A Ferretti, A Floris, G Fratesi, G Fugallo, R Gebauer, U Gerstmann, F Giustino, T Gorni, J Jia, M Kawamura, H-Y Ko, A Kokalj, E Kucukbenli, M Lazzeri, M Marsili, N Marzari, F Mauri, N L Nguyen, H-V Nguyen, A Otero de-la Roza, L Paulatto, S Ponce, D Rocca, R Sabatini, B Santra, M Schlipf, A P Seitsonen, A Smogunov, I Timrov, T Thonhauser, P Umari, N Vast, X Wu, and S Baroni, “Advanced capabilities for materials modelling with QUANTUM ESPRESSO,” *Journal of Physics: Condensed Matter* **29**, 465901 (2017).
- [30] The following pseudopotentials were used: Ca.pbe-spn-rrkjus_psl.0.2.3.UPF, Bi.pbe-dn-rrkjus_psl.0.2.2.UPF, and Bi.rel-pbe-dn-rrkjus_psl.0.2.2.UPF, <http://www.quantum-espresso.org/pseudopotentials/>.
- [31] John P. Perdew, Kieron Burke, and Matthias Ernzerhof, “Generalized Gradient Approximation Made Simple,” *Phys. Rev. Lett.* **77**, 3865–3868 (1996).
- [32] Stefano Baroni, Stefano de Gironcoli, Andrea Dal Corso, and Paolo Giannozzi, “Phonons and related crystal properties from density-functional perturbation theory,” *Rev. Mod. Phys.* **73**, 515–562 (2001).
- [33] P. B. Allen and R. C. Dynes, “Transition temperature of strong-coupled superconductors reanalyzed,” *Phys. Rev. B* **12**, 905–922 (1975).
- [34] Georg K.H. Madsen and David J. Singh, “BoltzTraP. A code for calculating band-structure dependent quantities,” *Computer Physics Communications* **175**, 67–71 (2006).
- [35] G. Grimvall, *The electron-phonon interaction in metals* (North-Holland, Amsterdam, 1981).
- [36] Derek A Stewart, “Ab initio investigation of phonon dispersion and anomalies in palladium,” *New Journal of Physics* **10**, 043025 (2008).
- [37] W. Kohn, “Image of the Fermi Surface in the Vibration Spectrum of a Metal,” *Physical Review Letters* **2**, 393–394 (1959).
- [38] Malgorzata Wierzbowska, Stefano de Gironcoli, and Paolo Giannozzi, “Origins of low-and high-pressure discontinuities of T_c in niobium,” arXiv preprint cond-mat/0504077 (2005).
- [39] See Fig. S2 in Supplemental Material for the phonon displacement patterns in A point.
- [40] W. L. McMillan, “Transition temperature of strong-coupled superconductors,” *Phys. Rev.* **167**, 331–344 (1968).
- [41] It is worth recalling here, that McMillan [40] for his T_c formula assumed $\mu^* = 0.13$ for transition metals and $\mu^* = 0.10$ for simple metals, whereas Allen and Dynes [33] recommended using their formula with $\mu^* = 0.10$ for transition metals, and even lower values, like $\mu^* = 0.09$, for simple metals. We consistently use $\mu^* = 0.10$ here. Taking $\mu^* = 0.13$ with McMillan formula and experimental T_c for CaBi₂ gives slightly larger $\lambda_{\text{expt}} = 0.59$.
- [42] See Fig. S3 in Supplemental Material for the phonon displacement patterns in Y point.

- [43] Jianyong Chen, “A Comprehensive Investigation of Superconductor KBi₂ via First-Principles Calculations,” *Journal of Superconductivity and Novel Magnetism* **31**, 1301–1307 (2018).
- [44] Shanshan Sun, Kai Liu, and Hechang Lei, “Type-I superconductivity in KBi₂ single crystals,” *Journal of Physics: Condensed Matter* **28**, 085701 (2016).
- [45] Rajveer Jha, Marcos A Avila, and Raquel A Ribeiro, “Hydrostatic pressure effect on the superconducting properties of BaBi₃ and SrBi₃ single crystals,” *Superconductor Science and Technology* **30**, 025015 (2016).
- [46] Neel Haldolaarachchige, SK Kushwaha, Quinn Gibson, and RJ Cava, “Superconducting properties of BaBi₃,” *Superconductor Science and Technology* **27**, 105001 (2014).
- [47] Bosen Wang, Xuan Luo, Kento Ishigaki, Kazuyuki Matsubayashi, Jinguang Cheng, Yuping Sun, and Yoshiya Uwatoko, “Two distinct superconducting phases and pressure-induced crossover from type-II to type-I superconductivity in the spin-orbit-coupled superconductors BaBi₃ and SrBi₃,” *Phys. Rev. B* **98**, 220506 (2018).
- [48] Masashi Kakihana, Hiromu Akamine, Tomoyuki Yara, Atsushi Teruya, Ai Nakamura, Tetsuya Takeuchi, Masato Hedo, Takao Nakama, Yoshichika Ōnuki, and Hisatomo Harima, “Fermi Surface Properties Based on the Relativistic Effect in SrBi₃ with AuCu₃-Type Cubic Structure,” *Journal of the Physical Society of Japan* **84**, 124702 (2015).
- [49] H. M. Tütüncü, Ertuğrul Karaca, H. Y. Uzunok, and G. P. Srivastava, “Role of spin-orbit coupling in the physical properties of LaX₃ (X = In, P, Bi) superconductors,” *Phys. Rev. B* **97**, 174512 (2018).
- [50] Xu Dong and Changzeng Fan, “Rich stoichiometries of stable Ca-Bi system: Structure prediction and superconductivity,” *Scientific reports* **5**, 9326 (2015).
- [51] Yasunobu Fujimori, Shin-ichi Kan, Bunjyu Shinozaki, and Takasi Kawaguti, “Superconducting and normal state properties of NiBi₃,” *Journal of the Physical Society of Japan* **69**, 3017–3026 (2000).
- [52] Jagdish Kumar, Anuj Kumar, Arpita Vajpayee, Bhasker Gahtori, Devina Sharma, PK Ahluwalia, S Auluck, and VPS Awana, “Physical property and electronic structure characterization of bulk superconducting Bi₃Ni,” *Superconductor Science and Technology* **24**, 085002 (2011).
- [53] Sommerfeld coefficient γ_{expt} may be renormalized by other effects than the electron-phonon interaction, however in such intermetallic compounds, with *s* and *p* electrons at the Fermi level, strong electron correlations or paramagnons are not expected to appear.

VIII. SUPPLEMENTAL MATERIAL

Fig. S1 shows in a convenient way relation between the primitive and conventional base-centered crystal cells of CaBi₂, which help to analyze Figs. S2 and S3.

Fig. S2 show phonon displacement patterns of all 18 phonon modes in A-point from the scalar-relativistic calculations, as in this case phonon linewidths are very large. Amplitude of modes is enlarged.

Fig. S3 show phonon displacement patterns of all 18 phonon modes in Y-point from the relativistic calculations. This point was chosen as it has large phonon linewidths in the relativistic case. Amplitude of modes is enlarged.

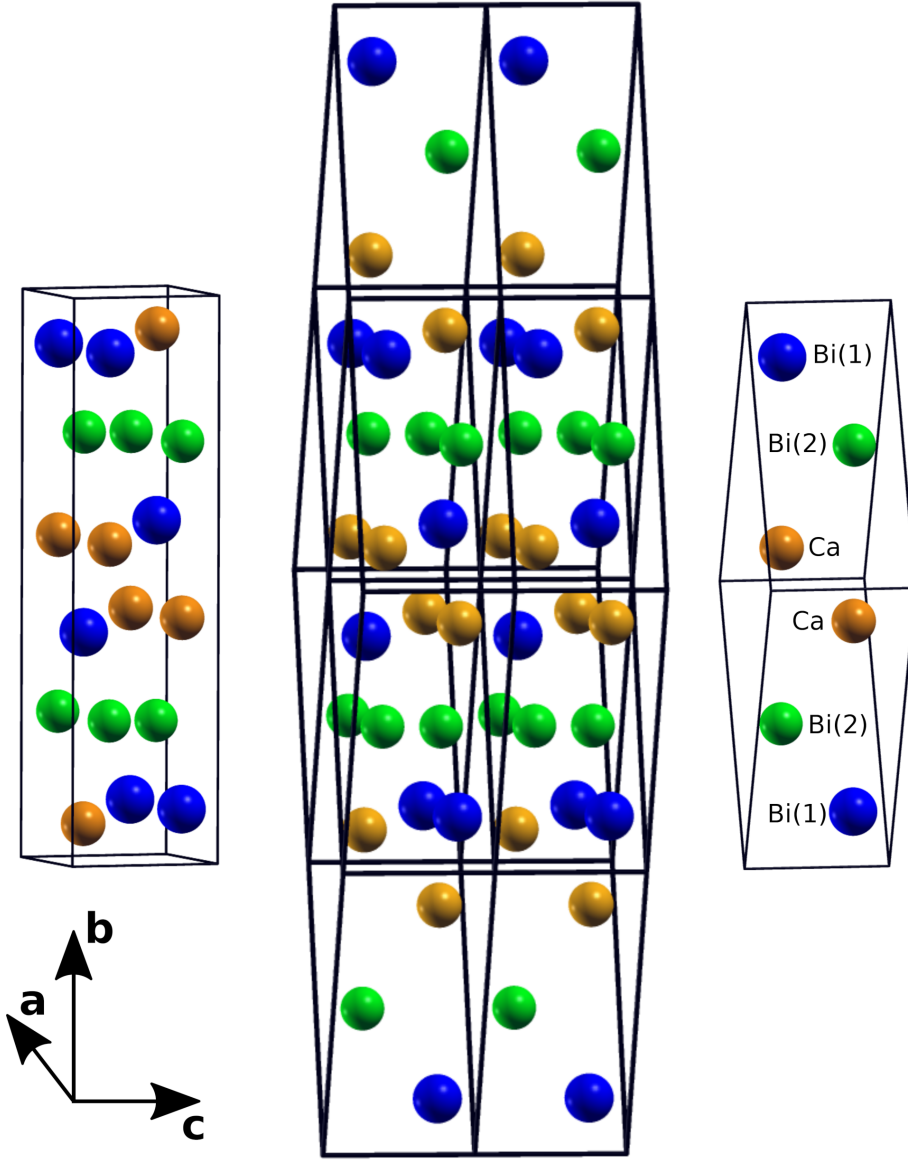


FIG. 8. Crystal structure of CaBi_2 . Left: Conventional unit cell, with Bi(1)-Ca and Bi(2) layers, perpendicular to b axis. Right: primitive cell. Middle: 2×2 primitive supercell, which shows the relation of primitive and conventional unit cells. a, c are the in-plane directions, whereas b is perpendicular to Bi and Ca-Bi layers.

AT q-POINT A, W/O SOC

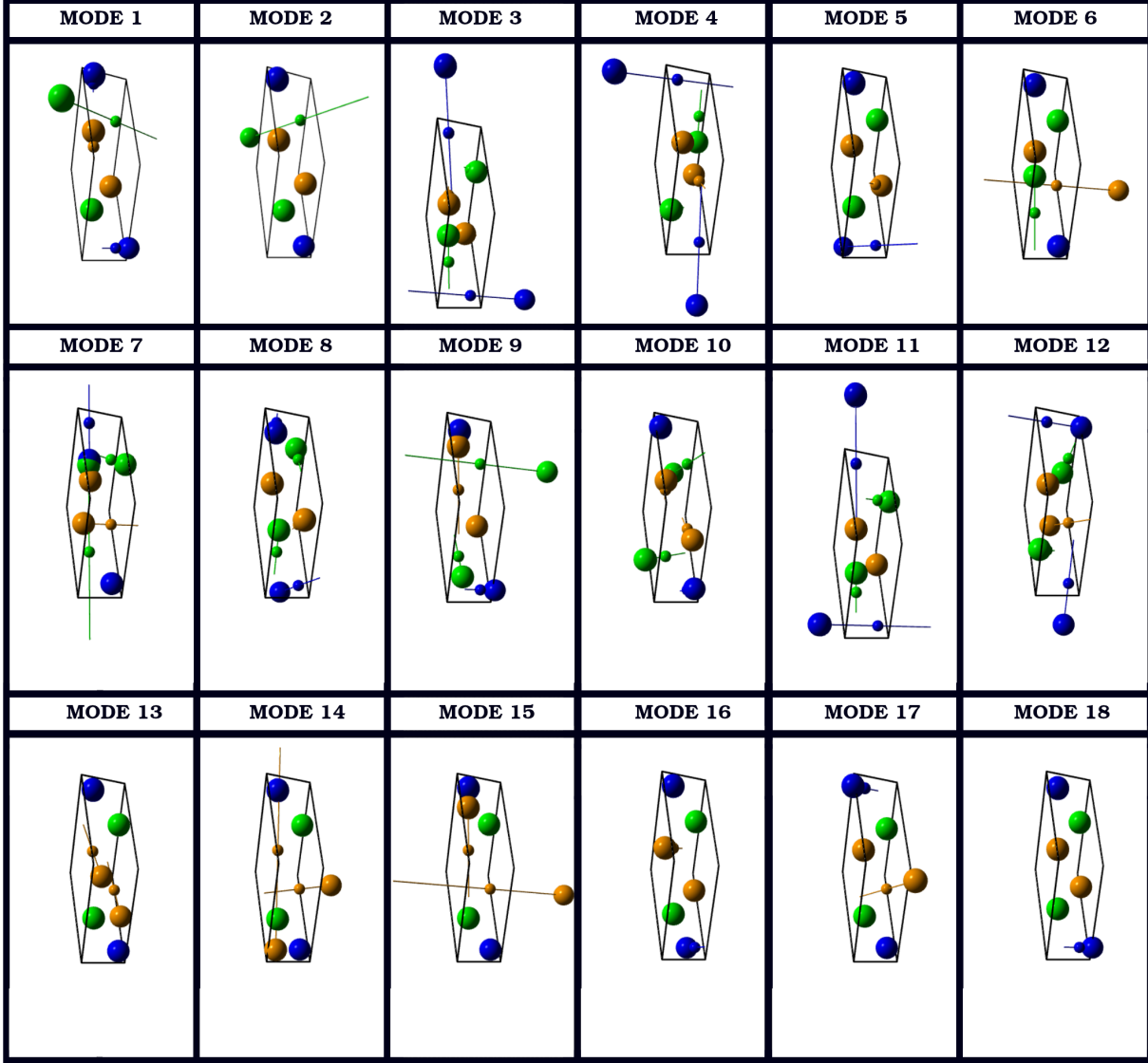


FIG. 9. Phonon displacement patterns of all 18 phonon modes in A-point from the scalar-relativistic calculations. Fig. S1 helps to identify which directions are in-plane or perpendicular to atomic planes.

AT q-POINT Y, WITH SOC

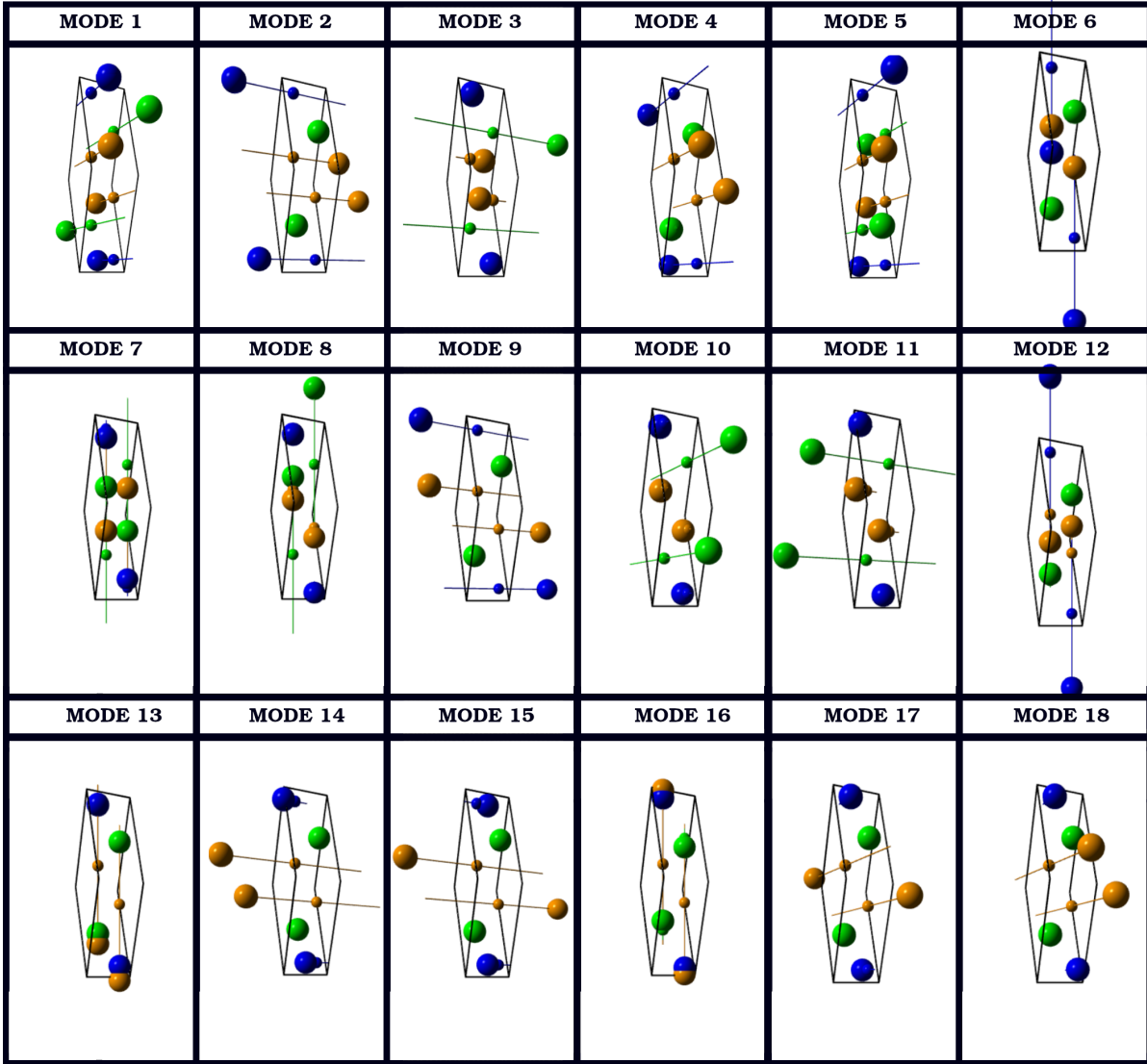


FIG. 10. Phonon displacement patterns of all 18 phonon modes in Y-point from the relativistic calculations. Fig. S1 helps to identify which directions are in-plane or perpendicular to atomic planes.